HAL
open science

Immersed boundary conditions for moving objects in turbulent flows with the lattice-Boltzmann method

Isabelle Cheylan, Julien Favier, Pierre Sagaut

To cite this version:

Isabelle Cheylan, Julien Favier, Pierre Sagaut. Immersed boundary conditions for moving objects in turbulent flows with the lattice-Boltzmann method. Physics of Fluids, 2021, 33 (9), pp.095101. 10.1063/5.0062575 . hal-03597108

HAL Id: hal-03597108

https://hal.science/hal-03597108v1

Submitted on 4 Mar 2022

HAL is a multi-disciplinary open access archive for the deposit and dissemination of scientific research documents, whether they are published or not. The documents may come from teaching and research institutions in France or abroad, or from public or private research centers.

L'archive ouverte pluridisciplinaire **HAL**, est destinée au dépôt et à la diffusion de documents scientifiques de niveau recherche, publiés ou non, émanant des établissements d'enseignement et de recherche français ou étrangers, des laboratoires publics ou privés.

Immersed boundary conditions for moving objects in turbulent flows with the lattice-Boltzmann method

Isabelle Cheylan,[a] Julien Favier, and Pierre Sagaut

AFFILIATIONS

Aix Marseille Univ, CNRS Centrale Marseille, M2P2 UMR 7340, 13451 Marseille Cedex 13, France

ABSTRACT

An immersed boundary method is coupled to a turbulent wall model and Large Eddy Simulation, within the Lattice-Boltzmann framework. The method is able to handle arbitrarily moving objects immersed in a high Reynolds number flow and to accurately capture the shear layer and near wall effects. We perform a thorough numerical study which validates the numerical method on a set of test-cases of increasing complexity, in order to demonstrate the application of this method to industrial conditions. The robustness and accuracy of the method are assessed first in a static laminar configuration, then in a mobile laminar case, and finally in a static and oscillating turbulent simulation. In all cases, the proposed method shows good results compared to the available data in the literature.

I. INTRODUCTION

In many industrial contexts, the simulation of flows at high Reynolds numbers involving unsteady structures is often encountered, from rotating objects in turbomachines to landing gears in aeronautics.[1,2] Several solutions have emerged over the years to tackle this issue: the grid can be deformed during the simulation as is done with the Arbitrary Lagrangian Eulerian (ALE)[3–5] or regenerated after each motion of the solid, leading to a cumbersome computation in both cases and limitations concerning the mesh size. An alternative is the overset method,[6,7] which consists of using two different meshes, one for the moving solid, and one for the fluid, coupled with accurate interpolations between the two meshes in order to translate the motion of the solid in the fluid. This method has been shown to produce very interesting results in the context of the lattice-Boltzmann method (LBM),[8] though being restricted to rotating geometries.

In this work, we propose to consider arbitrary moving objects immersed in turbulent flow conditions, using a robust and efficient method to impose boundary conditions on immersed geometries. Initially developed by Peskin in the 1970s,[9] the Immersed Boundary (IB) Method (IBM) consists of defining a volume force term on the boundary between the fluid and the solid, calculated to satisfy the no-slip boundary condition at the wall. A Lagrangian coordinate system is introduced to define the position of the solid, and the fluid quantities (velocity and force fields) are transferred back and forth from the fluid mesh, referred to as the Eulerian mesh, thanks to interpolation and spreading mathematical operators. These operators rely on delta functions defined on a narrow band across the boundary, typically three or four nodes. Despite a large usage of the immersed boundary method for laminar flows in contexts involving flexible, multiphase, magnetic, or porous boundary conditions,[10–17] it is less frequent to encounter studies at high Reynolds number flows, which can be done using Navier–Stokes solvers,[18] and more rarely using the lattice-Boltzmann framework, which is the framework here.

When dealing with high Reynolds number turbulent wall-bounded flows, modeling near wall turbulence, and more precisely the inner layer of the turbulent boundary layer, becomes a primary concern in many industrial fields, since this part of the flow governs most of the friction and heat/mass transfers at the wall. Since the mesh topology does not allow for a direct resolution of the turbulent inner layer dynamics, it must be modeled thanks to wall models that are in practice implemented as a new type of boundary condition at solid walls. To this end, different techniques exist to predict the mean velocity profile within the first cell near the wall. One of them is to consider that the tangential velocity profile follows a universal analytical law. The most commonly used law is the logarithmic law, which gives a relation between the tangential velocity, the distance to the wall, and

the friction velocity. The no-slip boundary condition can thus be replaced by the prescription of the wall shear stress. In this work, the power wall law,[19] which is an explicit wall model without any iterative procedure for the determination of the friction velocity, is combined with the immersed boundary method.

As proposed by Shi *et al.*,[20] one can distinguish different types of immersed boundaries: the sharp-interface immersed boundary method, where the solid and fluid phases are treated distinctly, and the diffuse-interface immersed boundary method, which is the case of this work, and in which the solid and fluid phases are treated indistinctly. In the former, the identification of the different types of points inside and outside the boundary is necessary, i.e., the fluid points, the solid points, and the interface points. When dealing with complex moving boundaries, this impacts the robustness and efficiency of the method, which can also suffer from spurious oscillations due to the spatial and temporal discontinuities near the wall. In the latter, a smooth transition between the fluid and solid phases is applied, hence bypassing these stability problems near the wall. Moreover, the diffuse interface IB method relies on a single mesh, meaning that there is no need to identify the different types of points, making the method more robust, especially in the moving boundary configuration. However, the diffuse-interface IB method has rarely been applied and combined to turbulent wall models, except recently in Ref. 20. They combined wall models with the diffuse interface immersed boundary and applied their method to turbulent flows, but only in a steady configuration. Here, we propose to further extend their approach by considering moving solids problems, and by using the Lattice-Boltzmann method. It is worth noting that the coupling of Wall Modeled Large Eddy Simulation (WMLES) with IB methods is pretty rare. Some illustrative examples are given in Table I.

The Lattice-Boltzmann Method (LBM) is based on the Boltzmann equation at a mesoscopic level and recovers the Navier–Stokes equations on the macroscopic level. Thanks to its automatically generated Cartesian mesh, as well as its very high parallel efficiency and very high numerical accuracy, the LBM has been gaining more and more interest in the industry. Practical applications range from the automotive industry, to the aerospace industry, but also civil engineering, among other applications. Here, we chose to combine the LBM to the immersed boundary, as both methods are naturally built on Cartesian meshes. It is worth noting that coupling wall models with LBM-IBM is still very rare, the only example to the knowledge of the authors being given recently in Ref. 27.

The novelty of this work is to propose (1) an implementation of Wall-Modeled LES within an LBM-IBM framework relying on the Hybrid Recursive Regularized (HRR) LBM collision model, (2) along with a validation for both steady and moving solid bodies at high Reynolds number flows.

TABLE I. Literature review on the coupling between wall-modeled LES and immersed boundary methods in the Navier–Stokes framework.

Reference	Type	Steady body	Moving body
21	WMLES	x	
22	WMLES	x	
23	Reynolds Averaged Navier Stokes (RANS)	x	
24	WMLES	x	x
25	WMLES	x	
26	RANS	x	

The present paper is organized as follows. First, the key features of the present LBM algorithm are given in Sec. II. Details of the implementation of the wall-model within the LBM-IBM framework are displayed in Sec. III. The computation of aerodynamic forces on the immersed boundary is also discussed in this section. A first validation of the implementation of LBM-IBM on both steady and laminar test cases is then given in Sec. IV. Application of the proposed WMLES-LBM-IBM technique to the flow around both steady and oscillating square cylinders is then discussed in Sec. V. Conclusions are drawn in Sec. VI

II. KEY FEATURES OF THE PRESENT LBM ALGORITHM FOR LES

A. HRR-collision-model

The typical D3Q19 lattice discretization is used in this work because it is well-suited to simulate athermal weakly compressible flows, even though the LBM is inherently compressible. The weighting coefficients for the D3Q19 quadrature are $\omega_0 = \frac{1}{3}$ for the center, $\omega_{1\ldots6} = \frac{1}{18}$ for the faces, and $\omega_{7\ldots18} = \frac{1}{36}$ for the edges

$$\boldsymbol{c_i} = \begin{cases} (0,0,0), & \mathrm{i} = 0, \\ (\pm1,0,0),(0,\pm1,0),(0,0,\pm1), & \mathrm{i} = 1-6, \\ (\pm1,\pm1,0),(\pm1,0,\pm1),(0,\pm1,\pm1), & \mathrm{i} = 7-18. \end{cases} \tag{1}$$

The macroscopic quantities (density ρ, momentum ρu_α, and momentum flux tensor $\Pi_{\alpha\beta}$) are then computed from the velocity moments of the distribution functions as follows:

$$\begin{cases} \rho = \sum_i f_i, \\ \rho u_\alpha = \sum_i c_{i,\alpha} f_i, \\ \Pi_{\alpha\beta} = \sum_i c_{i,\alpha} c_{i,\beta} f_i. \end{cases} \tag{2}$$

The Lattice-Boltzmann equation, discretized in space, time, and velocities, is given by

$$f_i(\boldsymbol{x} + \boldsymbol{c_i}\Delta_t, t + \Delta_t) = f_i^{eq}(\boldsymbol{x}, t) + \left(1 - \frac{1}{\tau}\right) f_i^{neq}(\boldsymbol{x}, t) + \frac{1}{2} h_i(\boldsymbol{x}, t), \tag{3}$$

$$h_i = \omega_i \left(1 - \frac{1}{2\tau}\right) \left[\frac{\boldsymbol{c_i} - \boldsymbol{u}}{c_s^2} + \frac{\boldsymbol{c_i}.\boldsymbol{u}}{c_s^4} \boldsymbol{c_i}\right] . \boldsymbol{g}, \tag{4}$$

where $\boldsymbol{g}$ denotes an external macroscopic volumic force. The equilibrium function is written

$$f_i^{eq} = \omega_i \left[\rho + \frac{c_{i\alpha}\rho u_\alpha}{c_s^2} + \frac{a_{\alpha\beta}^{(2),eq} H_{i\alpha\beta}^{(2)}}{2c_s^4} + \frac{a_{\alpha\beta\gamma}^{(3),eq} H_{i\alpha\beta\gamma}^{(3)}}{6c_s^6}\right], \tag{5}$$

where $H_{i\alpha\beta}$ and $H_{i\alpha\beta\gamma}$ are, respectively, the second and third order Hermite polynomials. The non-equilibrium distribution function is also expanded in Hermite polynomials and reconstructed by a Recursive Regularized Bhatnagar-Gross-Krook (BGK) LBM,[28,29]

$$f_i^{neq} = \omega_i \left[\frac{a_{\alpha\beta}^{(2),neq} H_{i\alpha\beta}^{(2)}}{2c_s^4} + \frac{a_{\alpha\beta\gamma}^{(3),neq} H_{i\alpha\beta\gamma}^{(3)}}{6c_s^6}\right]. \tag{6}$$

In the present approach, the non-equilibrium coefficients $a_{\alpha\beta}^{(2),neq}$ and $a_{\alpha\beta\gamma}^{(3),neq}$ are evaluated with the hybrid recursive collision model introduced in Ref. 28. This model is used to enhance numerical stability, as well as enforce a traceless lattice-Boltzmann tensor by removing its trace. It is observed to yield accurate and robust results for a broad range of applications and flow physics, e.g., Refs. 30–34.

In this approach, when an external force g is taken into account, such as the immersed boundary force, the macroscopic momentum is modified as

$$\rho \boldsymbol{u} = \sum_i \boldsymbol{c}_i f_i^{eq} + \frac{\boldsymbol{g}}{2}\Delta_t. \tag{7}$$

B. Shear-improved Smagorinsky subgrid model

To account for the unresolved scales of motion in the turbulent case, a subgrid model is used, and more precisely, a variant of the Smagorinsky model called the "shear-improved Smagorinsky" proposed in Ref. 35. In this model, the calculation of the turbulent viscosity is

$$\nu_t = (C_S^2 \Delta x)^2 (|S| - \mathcal{S}), \tag{8}$$

with C_S the Smagorinsky constant, Δx the local grid spacing, and $|S|$ the norm of the rate of strain tensor. The correcting term $\mathcal{S}$ is the norm of the low-pass filtering (in time) of the rate of strain tensor. This filtering is explained in detail in Ref. 35 and is independent of the test case.

In the LBM, the turbulent viscosity is taken into account in the calculation of the physical relaxation time τ^S,

$$\tau^S = \frac{\nu + \nu_t}{c_s^2} + \frac{1}{2}\Delta t, \tag{9}$$

with ν and ν_t the molecular viscosity and turbulent viscosity, respectively.

III. IMPLEMENTATION OF THE WALL MODEL IN THE LBM-IBM FRAMEWORK

A. Implementation of the immersed boundary method

The immersed boundary force is a fictitious force which represents the effects of the solid on the flow. The solid boundary is described by a set of Lagrangian markers X_k, whereas the Eulerian fluid nodes are denoted by x_i. Capital letters indicate the variables at the Lagrangian points and $\boldsymbol{u}^\star$ is the predicted velocity without the presence of a solid. The main advantage of the immersed boundary method is that the motion of the solid can be described with a single mesh and a moving frontier across this original mesh. Thus, there is no need to deform the mesh nor recreate a new mesh during the computation, which are well-known computationally expensive procedures. The algorithm of the IB method, without any wall law, is described in this section, as derived in Refs. 13 and 36.

(1) Update of the position of the lagrangian markers $\boldsymbol{X_k}$ and the velocity of the solid $\boldsymbol{U^d}$.
(2) Algorithm of the LBM without solids on the Eulerian fluid nodes.
(3) Interpolation of ρ and $\boldsymbol{u}$ on the lagrangian markers $\boldsymbol{X_k}$

$$I[\rho](\boldsymbol{X_k}) = \sum_{x_i} \rho(\boldsymbol{x_i})\delta(\boldsymbol{x_i} - \boldsymbol{X_k})\Delta S_i. \tag{10}$$

(4) Computation of the immersed boundary force

$$\boldsymbol{G}(\boldsymbol{X_k}) = \frac{2}{\Delta t}(I[\rho]\boldsymbol{U^d} - I[\rho\boldsymbol{u}^\star]). \tag{11}$$

(5) Spreading of the force on the surrounding Eulerian fluid nodes

$$\boldsymbol{g}(\boldsymbol{x_i}) = S[\boldsymbol{G}](\boldsymbol{x_i}) = \sum_{X_K} \boldsymbol{G}(\boldsymbol{X_k})\delta(\boldsymbol{x_i} - \boldsymbol{X_k})\Delta S_k. \tag{12}$$

(6) Update of the velocity $\boldsymbol{u}$ [Eq. (7)] and the distribution function f_i [Eq. (3)] in the LBM.

$\boldsymbol{G}$ is the immersed boundary force expressed in the Lagrangian space, and $\boldsymbol{g}$ is the same force expressed in the Eulerian space, used in Eqs. (4) and (7). In the interpolation or spreading operators, $\Delta S_i = \Delta x \Delta y \Delta z$ is the cell surface expressed in the Eulerian space, and $\Delta S_k = \Delta l_k \epsilon$ is a local surface element expressed in the Lagrangian space, with Δl_k the local distance between two solid points and ϵ a boundary width usually set to unity, as done here. $\delta(x)$ is a mollifier or a smooth approximation of the Dirac delta function. It is the discrete equivalent of the Dirac delta function which serves to transport information from the Lagrangian space to the Eulerian space and vice versa. Here, the mollifier function used in the interpolation and spreading steps is defined as

$$\delta(r) = \begin{cases} \frac{1}{2d}\left(1 + \cos\left(\frac{\pi r}{d}\right)\right), & |r| \le d, \\ 0, & |r| > d, \end{cases} \tag{13}$$

where d is the radius of the smoothed delta function, set to 3/2 here.

B. Combination of the wall model with the immersed boundary

In order to deal with turbulent wall bounded flows, a turbulent wall law is coupled with the immersed boundary method, following the approach proposed by Shi *et al.*[20] A fictitious node on the line normal to the wall is defined and located at an arbitrarily fixed distance to the wall. This fictitious node, called Ref point in this work is located at a distance of 2.5 Δx from the wall in the present work, where Δx is the local grid size. The tangential velocity at the Ref point is calculated using the immersed boundary interpolation operator. The point Q, located at $\Delta x/4$ as indicated by Shi *et al.*,[20] serves as an auxiliary point instead of point S on the wall, to calculate the wall shear stress. In Fig. 1, the dotted square line represents the application field of the δ mollifier function [Eq. (13)].

The algorithm for the wall law coupled to the immersed boundary is given by:

(1) Computation of the normal to the boundary, using point Ref at a distance 2.5 Δx, and point Q at a distance $\Delta x/4$.
(2) Interpolation of ρ and $\boldsymbol{u}$ on Ref.
(3) Computation of the friction velocity u_τ with the power wall law.
(4) Computation of the wall shear stress and the immersed boundary force on point Q.
(5) Spreading of the force from the point Q on the surrounding Eulerian fluid nodes.

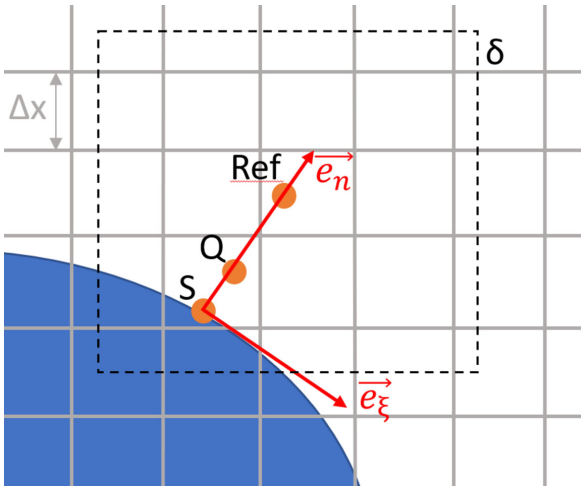

FIG. 1. Schematic diagram of the wall law.

The explicit power-law is well suited for a simplified near-wall treatment at high Reynolds numbers using Cartesian grids. The use of a wall model on a Cartesian grid is simplified by using a power-law model because it does not require an iterative procedure to calculate the friction velocity, contrary to the logarithmic law.[19] The methodology consists of first applying the wall model to a point where the velocity is predicted, thanks to the interpolation operator in our case, in order to calculate the friction velocity from the wall model. For the application of the power-law here, the reference point (Ref point defined in Fig. 1) is used. The power law can be applied at the Ref point

$$u^+_{Ref} = \begin{cases} y^+_{Ref} & \text{if } y^+_{Ref} \leq y^+_c, \\ A(y^+_{Ref})^B & \text{if } y^+_{Ref} > y^+_c, \end{cases} \tag{14}$$

with B = 1/7, A = 8.3, and $y^+_c = y_c u_\tau/\nu = 11.81$. The wall shear stress is then deduced as: $\tau_w = \rho u_\tau^2$ and used in the immersed boundary force at the point Q.

The immersed boundary force is decomposed in the local orthogonal coordinate system as $\boldsymbol{G} = G_\xi \boldsymbol{e_\xi} + G_n \boldsymbol{e_n}$ where G_ξ is the tangential component and G_n is the normal component, which are calculated separately. $\boldsymbol{e_\xi}$ is the tangential vector and $\boldsymbol{e_n}$ is the normal vector to the solid surface in Fig. 1. By integrating the momentum equation along the normal direction to link the effective body force to the wall shear stress, we find

$$\int_0^{\Delta x/2} \boldsymbol{g}.\boldsymbol{e_\xi}\, \mathrm{d}x = \int_0^{\Delta x/2} \left(\frac{\partial \boldsymbol{u}}{\partial t} + \boldsymbol{u}.\nabla \boldsymbol{u} + \nabla p - \frac{1}{Re}\nabla^2 \boldsymbol{u} \right).\boldsymbol{e_\xi}\, \mathrm{d}x. \tag{15}$$

The integration is done between points S and Ref, more precisely between 0 and $\frac{\Delta x}{2}$, following the findings of Shi *et al.*[20] showing that the location of point Q at a distance of $\Delta x/4.0$ from the wall yields good results for all the simulations in their work. Then, the previous equation can be expressed in terms of the variables at the Lagrangian points by integrating the viscous terms between the wall and Ref point, and using the mean value theorem for integrals to calculate the other terms

$$G_\xi(Q) = \left(\frac{\partial(\boldsymbol{U}.\boldsymbol{e_\xi})}{\partial t} + \boldsymbol{U}.\nabla \boldsymbol{U}.\boldsymbol{e_\xi} + \frac{\partial P}{\partial \xi} \right)\Bigg|_{\Delta x/4} + \frac{\tau_w}{\Delta x/2} - \frac{\tau_{\Delta x/2}}{\Delta x/2}. \tag{16}$$

The capital letters indicate the variables at the Lagrangian points. ξ indicates the coordinate along the tangential vector $\boldsymbol{e_\xi}$. τ_w and $\tau_{\Delta x/2}$ are the shear stresses at the wall and at the distance $\Delta x/2$ from the wall, respectively. As exposed in Ref. 20, for the wall-modeled LES of a turbulent flow, the right-hand side of Eq. (16) can be approximated by the dominant wall shear stress term as follows:

$$G_\xi(Q) = 2\frac{\tau_w}{\Delta x}, \tag{17}$$

$$G_n(Q) = \frac{2}{\Delta t}\left(I[\rho]\boldsymbol{U_n^d} - I\left[\rho \boldsymbol{u_n^*}\right]\right). \tag{18}$$

The tangential and normal components of the effective body forces are both computed at the auxiliary point Q near the wall instead of Point S on the wall. The Lagrangian points near the wall, denoted as Q, are the new Lagrangian points introduced in this work as a surrogate wall. In the case of the moving boundary, the relative velocity $\boldsymbol{U} = \boldsymbol{U}^{\mathrm{Ref}} - \boldsymbol{U^d}$ is used in the wall law.

C. Drag force computation

To compute the aerodynamic forces acting on an immersed object, two methods are classically used. The most widely used one, referred to as the Near-Field method here, is based on the integration of the pressure and viscous stresses acting on the surface of the object. Depending on the surface mesh of the object and on the interpolations used along the surface, the accuracy of this first method can be significantly altered.

The second method relies on the integration of the momentum equation on a far away surface enclosing the body, hence the name "Far-Field method." It is often used in the car industry to calculate the aerodynamic forces.[37,38] The main advantage of this second method is that there is no need for an accurate description of the surface, and it also allows one to decompose the drag into its physical components.[39,40] Nevertheless if the computation is unsteady, the far-field method becomes cumbersome numerically because a volume integral is needed at each time step.

In this work, as we use the immersed boundary method, it is more convenient to compute directly the aerodynamic forces, denoted as $\boldsymbol{F}$, by integrating the immersed boundary force on the Lagrangian space, denoted Ω or the Eulerian space, denoted Γ

$$\boldsymbol{F} = \int_\Omega \boldsymbol{G}(\boldsymbol{X_k})d\Omega = \int_\Gamma \boldsymbol{g}(\boldsymbol{x_i})d\Gamma. \tag{19}$$

IV. VALIDATION OF THE BASE LBM-IBM SOLVER

To validate our approach, we examine different test cases of increasing complexity. First, the immersed boundary is assessed on a static cylinder immersed in a flow at Reynolds number 100 and shows good results on the comparison of the aerodynamic forces. The second test case focuses on a cross-flow oscillating cylinder at Reynolds number 185, making it possible to use our approach in a moving solid configuration. The oscillating frequency is based on the natural vortex shedding frequency of the cylinder in order to observe the lock-in phenomenon.

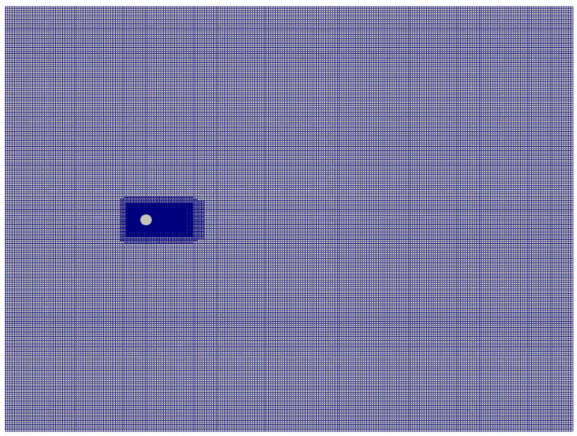

FIG. 2. Computational mesh with refined zones around the cylinder.

A. 2D laminar flow at Re = 100 around a fixed cylinder

The laminar flow around a cylinder at a Reynolds number 100 is studied. The computational domain is quasi 2D and is composed of approximately 200 000 nodes. There are 4 grid sizes shown in Fig. 2, the ratio $D/\Delta x$ is equal to 20, and the cylinder is located at 12D from the inlet, 38D from the outlet, and at 8D from the top and bottom, with D the cylinder diameter and Δx the minimum mesh size. The HRR collision model is used, and the instantaneous velocity field is shown in Fig. 3.

The results in Table II show a gap with literature results within 3.6%–10% difference on the mean drag, and 1%–3% on the Strouhal number defined by $St = \frac{fD}{V}$, where f is the vortex shedding frequency, D is the diameter, and V is the reference velocity. An estimation of Cl' close to literature results (0%–10%) is also obtained, which shows the very good agreement of the present results with the literature.

B. 2D laminar flow at Re = 185 around an oscillating cylinder

We now consider an unsteady configuration for the solid: the flow around an oscillating cylinder at a Reynolds number of 185. The motion of the cylinder center along the vertical direction is expressed as $y_{cyl}(t) = -A_e \sin(2\pi f_e t)$ based on Guilmineau and Queutey's study,[41] where A_e is the oscillating amplitude and f_e is the exciting frequency. The oscillation amplitude is normalized by the cylinder diameter and the following values are tested: 0.2, 0.3, 0.4, and 0.5. The frequency ratio, i.e., $f_r = f_e/f_o$, ranges from 0.8 to 1.2, where f_o is the natural shedding frequency of a fixed cylinder at a Reynolds number of 185. This test case serves as a reference case to study the phenomenon of vortex switching: Ongoren and Rockwell[42] experimentally showed that the switch of vortex formation position occurs according to the oscillation frequency. When the cylinder reaches the maximum amplitude of oscillation, if the exciting frequency exceeds the natural vortex shedding frequency, the vorticity concentration abruptly switches to the opposite side of the cylinder and the vortex formed on one side of the cylinder is shed on the opposite side.

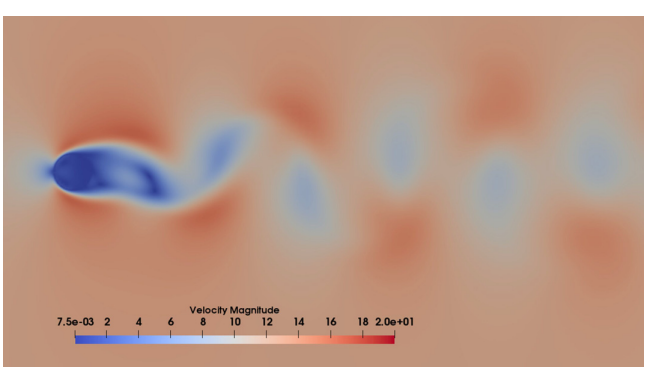

FIG. 3. Instantaneous velocity field around a cylinder at Re = 100.

TABLE II. Results on the static cylinder at Re = 100.

Study	$\overline{C_d}$	St	C_l'
Braza *et al.* (1986)	1.28	0.16	0.29
Zhou *et al.* (1999)	1.48	0.162	0.31
Shen *et al.* (2009)	1.38	0.166	0.33
Bourguet *et al.* (2014)	1.32	0.164	0.32
Gsell *et al.* (2021)	1.37	0.164	0.34
Present	1.42	0.166	0.33

The computational domain is quasi 2D and is composed of approximately 340 000 nodes. There are 4 grid sizes, the ratio $D/\Delta x$ is equal to 20, and the cylinder is located at 12D from the inlet, 38D from the outlet, and at 8D from the top and bottom, with D the cylinder diameter and Δx the minimum mesh size.

In order to obtain the primary and secondary frequencies of the vortex shedding cycle, a Fast Fourier transform operation is performed on the time history of the lift coefficient C_l. The normalized vortex shedding frequency f_s by the natural shedding frequency f_o as a function of as a function of the f_r for different A/D = 0.3, where $f_{s,P}$ and $f_{s,S}$ are the primary and secondary frequencies of f_s, respectively, is shown in Fig. 4.

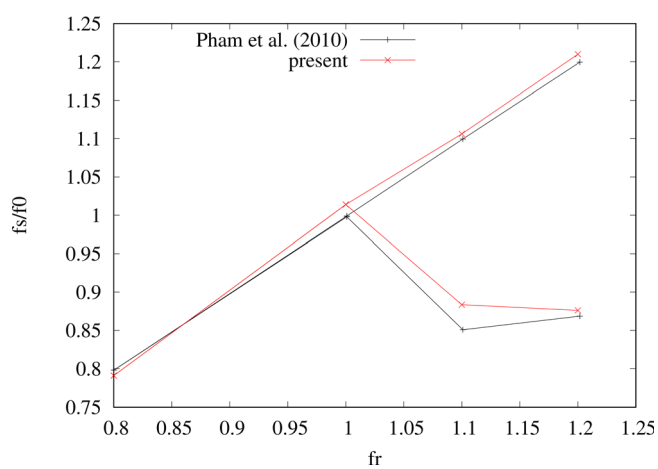

FIG. 4. Normalized vortex frequency.

The maximum error amplitude on the frequencies compared to Pham *et al.*[43] is around 3.5%, for $f_r = 1.1$ and A/D = 0.3. The phenomenon of vortex switching is well captured as shown by the bifurcation at $f_r = 1$ in Fig. 4.

Regarding the time-averaged values, the drag coefficient for $f_r = 1$ and A/D = 0.2 is compared to previous studies in the following table (Table III):

The fluctuating components of the force can also be calculated and compared to the reference data, for $f_r = 0.8$ and A/D = 0.2, we find $C_{d,RMS} = 0.046$ against $C_{d,RMS} = 0.053$ in Pham *et al.*[43] This very good agreement with reference data shows the accuracy of the proposed method.

V. VALIDATION THE WMLES-LBM-IBM

This section is dedicated to the validation of the WMLES-LBM-immersed boundary condition (IBC) approach. As a first case, the well-known case of the flow around a steady square cylinder at Reynolds 22 000 is addressed. In a second step, transversely oscillating square cylinder configurations are considered.

A. Steady square cylinder case at Re = 22 000

This second test case focuses on the flow past a steady square cylinder at a Reynolds number of 22 000 which is a very popular test case in the field of LES of the flow around bluff bodies.[44,45] Flow past a square cylinder is a test case of great interest for many fields of applications, including prediction of wind loads on buildings[46] or the VIV phenomenon "vortex induced vibration (VIV)," which is one of the main causes for structural fatigue and failure.

The instantaneous flow features are illustrated in Figs. 5 and 6 in which pressure and velocity fields are displayed, respectively. As expected for this flow configuration, it is seen that the shear layer separation occurs at the leading edge corners and that the near wake is made of small turbulent structures modulated by large-scale structures associated with the alternated vortex shedding originating in the interaction between the two separated shear layers, according to Gerrard's theory. It is observed that the flow does not exhibit spurious wiggles and that small scale structures are present in the flow, demonstrating the accuracy and the robustness of the proposed method for LES.

A first quantitative validation is carried out by looking at global integrated quantities (see Table IV), such as aerodynamics forces and the topology of the time-averaged recirculation bubbles in the near wake. A very good agreement with reference data is observed, showing the accuracy of the present simulation.

A finer validation of the WMLES-LBM-IBM is done looking at the separated shear layers on the top side of the cylinder (Figs. 7 and 8) and in the near wake (see Fig. 9). It is observed that the separation bubble on the top side of the cylinder is accurately predicted, since the separated shear layer has a good thickness and that it is located at the correct distance from the solid wall, showing that the wall model is accurately implemented within the present LBM-IBM framework, since viscous effects, wall pressure effects, and Kelvin–Helmholtz instabilities are accurately predicted in the near wall region.

It is also seen in Fig. 9 that the mean velocity field is very accurately predicted in the near wake, showing that separated shear layer dynamics is very well captured on the top and bottom sides of the cylinder and that the shear layer evolution downstream the trailing edge corners is also well predicted.

TABLE III. Results on the oscillating cylinder at Re = 185.

Study	$\overline{C_d}$
Guilmineau and Queutey (2002)	1.52
Chen *et al.* (2020)	1.55
Present	1.6

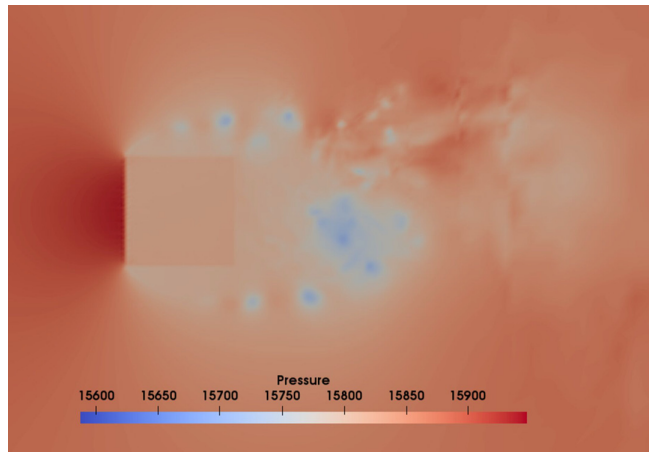

FIG. 5. Pressure field around the square cylinder at Re = 22 000.

B. Oscillating square cylinder case at Re = 22 000

We now consider a moving solid in a turbulent flow, simulated by a Large Eddy Simulation Lattice-Boltzmann solver coupled to a power wall law for the near wall turbulence. The square cylinders are forced to oscillate in a prescribed sinusoidal motion at reduced velocity $U_r = U/fD = 7.7 = 1/St_0$ (with U, f, and D the upstream velocity,

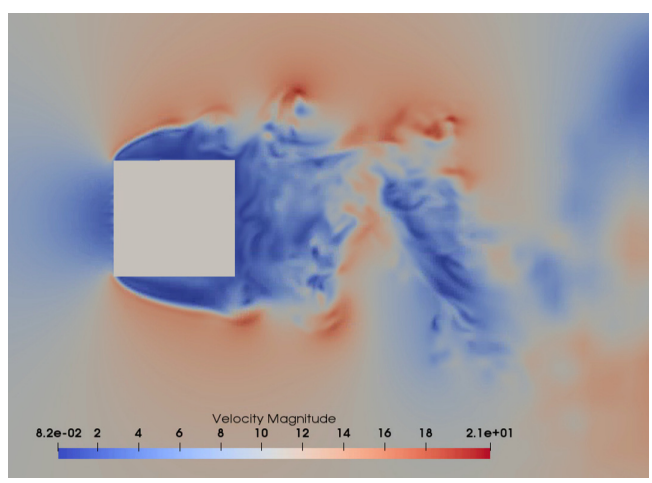

FIG. 6. Velocity field around the square cylinder at Re = 22 000.

TABLE IV. Time-averaged global parameters for the flow around the steady square cylinder at Re = 22 000: mean drag coefficient $\overline{C_d}$, dominant Strouhal number *St*, rms of the drag coefficient $C_{d,RMS}$, and length of the time-averaged near wake recirculation region $L_f(D)$.

Study	$\overline{C_d}$	St	$C_{d,RMS}$	$L_f(D)$
Lyn *et al.* (experiment, 1995)	2.11	0.13	...	1.37
Minguez *et al.* (experiment, 2011)	2.1	0.13	...	...
Chen *et al.* (LES, 2020)	2.246	0.135	0.14	1.1
Cao and Tamura (LES, 2016)	2.11–2.30	0.126–0.138	0.086–0.273	1.03–1.25
Present	2.09	0.14	0.143 48	1.009

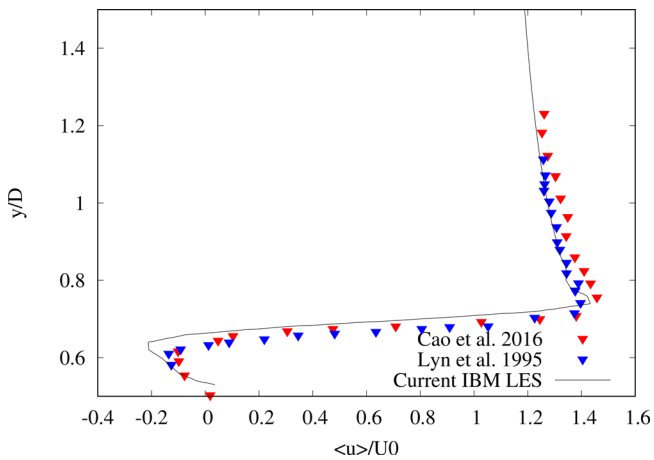

FIG. 7. Profiles of time and spanwise averaged streamwise velocity ⟨*u*⟩/U0 at x/D = −0.25. Comparison with experimental measurements (Lyn *et al.*, 1995) and LES (Cao *et al.*, 2016).

the cylinder oscillation frequency, and the cylinder size, respectively), which corresponds to the resonance point of the lock-in regime. Here, St_0 denotes the Strouhal number of the vortex shedding of the steady cylinder case.[47,48] In this regime, the cylinder wake is perfectly in phase with the cylinder oscillation. In the case of a freely oscillating cylinder, this regime is a stable one, the net energy transfer being from the cylinder to the fluid.[49] Two amplitude ratios $A/D = 0.05$ and 0.1 based on a cylinder height D are studied. At such small reduced amplitudes, the main effect of the cylinder is to modify the dynamics of the separated shear layers that develop on its top and bottom side, but there is no direct large scale forcing of the amplitude of the vortex shedding. Therefore, in such regimes, the capability of the present LBM-IBM implementation of the wall model to recover both the generation of vorticity but also the forcing of the separated shear layers by the solid wall oscillations will be assessed.

The computational domain is 3D and composed of 3 763 752 nodes; the simulation is run on 352 processors. There are 5 grid sizes (Fig. 2), and the ratio $D/\Delta x$ is equal to 50.

Some global parameters related to aerodynamics forces are displayed in Table V. The decrease in the mean drag force when the oscillating amplitude is increased has already been reported in Ref. 50. They studied the turbulent flow around a circular cylinder at a Reynolds number of 10^5 and observed that the inertial effects dominate when the shedding frequency is locked to the body oscillation frequency. This means that as the amplitude of the body oscillation increases, the drag coefficient decreases because the highest pressures are observed in the front and at the rear of the cylinder, almost canceling each other out which leads to a decreasing drag force. Table VI shows the results obtained by Hirata *et al.*,[50] keeping the oscillation

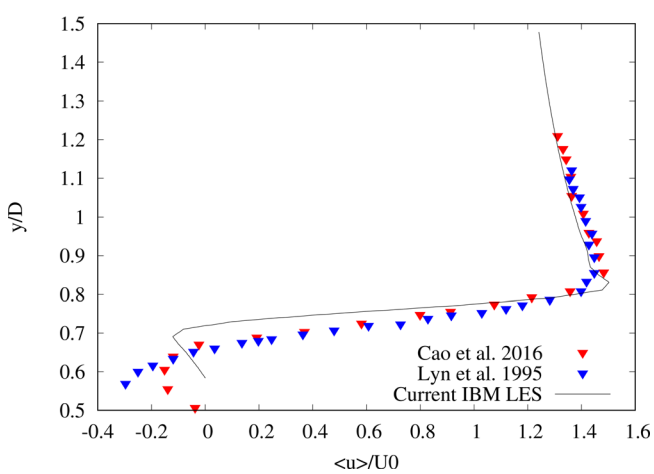

FIG. 8. Profiles of time and spanwise averaged streamwise velocity ⟨*u*⟩/U0 at x/D = 0. Comparison with experimental measurements (Lyn *et al.*, 1995) and LES (Cao *et al.*, 2016).

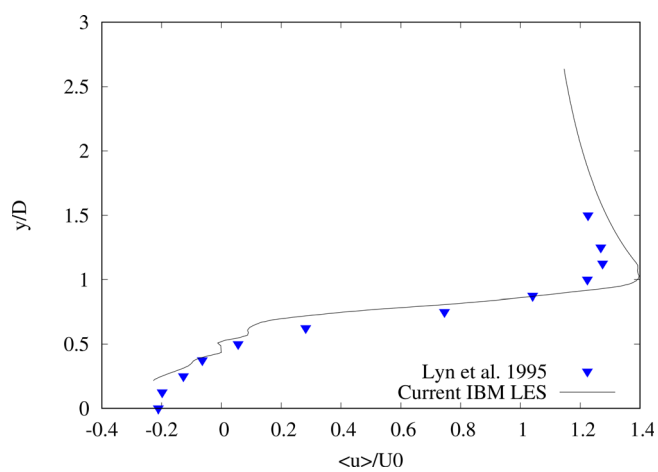

FIG. 9. Profiles of time and spanwise averaged streamwise velocity ⟨*u*⟩/U0 at x/D = 0.875. Comparison with experimental measurements (Lyn *et al.*, 1995).

TABLE V. Results on the oscillating square cylinder at Re = 22 000.

Case	U_r	$\overline{C_d}$	$C_{d,RMS}$	$\overline{C_l}$	$C_{l,RMS}$
Fixed	0.0	2.09	0.143 48	0.02	0.65
A/D = 0.05	7.7	2.005	0.076	0.000 82	1.086
A/D = 0.1	7.7	1.905	0.104	0.008	2.073

TABLE VI. Results on the oscillating circular cylinder taken from Ref. 50.

Cases from Hirata *et al.*[50]	$\overline{C_d}$
A/D = 0.01	1.278
A/D = 0.05	1.095
A/D = 0.1	0.886

frequency of the body constant with a value of St = 0.239, which corresponds to the regime where the shedding frequency is locked to the body oscillation frequency. They observe that as the amplitude of oscillation increases the drag coefficient decreases.

The same phenomenon is observed here: the maximum drag force is obtained for the fixed cylinder, and it decreases as the oscillating amplitude increases. We also notice that the order of magnitude of the decrease in the drag force is similar to the results obtained by Hirata *et al.*[50]

The fluctuating lift is observed to be a growing function of the reduced amplitude, which is in agreement with experimental observations for this range of variations of A/D in the lock-in regime. The computed values are coherent with experimental observations reported in Refs. 47, 48, and 51 for oscillating square cylinders in the turbulent regime as can be seen in Table VII for A/D = 0.1.

It is worth noting that experimental data exhibit a significant dispersion, but the present numerical results are within the experimental uncertainty.

A deeper insight into the flow physics is obtained looking at the time histories of the drag and lift coefficients (Figs. 10 and 11, respectively). The turbulent character of the flow is observed to yield a non-sinusoidal evolution of both drag and lift. The lift fluctuations are observed to be mostly governed by large scales of the near-wake region, i.e., the large-scale vortex shedding that occurs at the main Strouhal number. Drag fluctuations are more sensitive to small scales and details of the separated shear layers, and then exhibit a more complex behavior but also a stronger sensitivity to the cylinder oscillations in the present regime.

Bearman *et al.*[47,48] showed that the phase angle between the cylinder position and the lift is a growing function of A/D. The same

TABLE VII. Comparison of the fluctuating lift coefficient with experiments.

Cases	$C_{l,RMS}$
Bearman and Obasaju, 1982[47]	1.8
Obasaju *et al.*, 1983[51]	1.9
Present	2.073

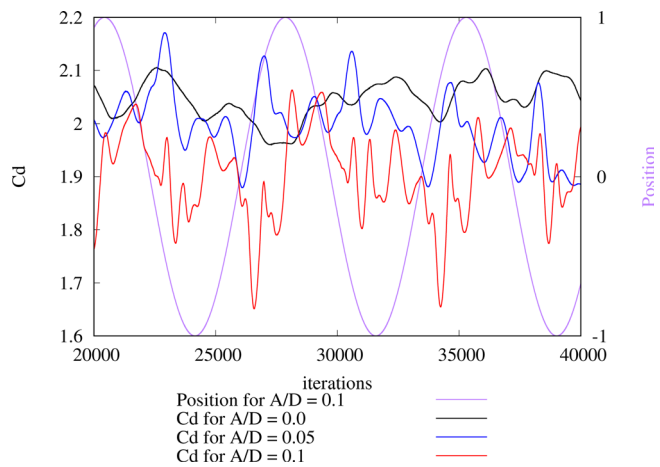

FIG. 10. Time history of the drag coefficient and position of the cylinder for the static and oscillating cases.

phenomenon can be observed in Fig. 11, showing that the present model correctly reproduces the overall experimental behavior of the oscillating square cylinder.

The overall satisfactory agreement of computed results in both oscillating cylinder case shows that the present WMLES-LBM-IBM can accurately capture the turbulent flow physics for moving bluff bodies.

VI. CONCLUSIONS

An original WMLES-LBM-IBM has been proposed and assessed on several test cases exhibiting both steady and moving solid boundaries. To the knowledge of the authors, this is the first time that such a method is equipped with the Hybrid Recursive Regularized collision model.

Validation results have demonstrated both the accuracy and the robustness of the present method. More precisely, simple 2D laminar test cases have shown the capability of the method to accurately

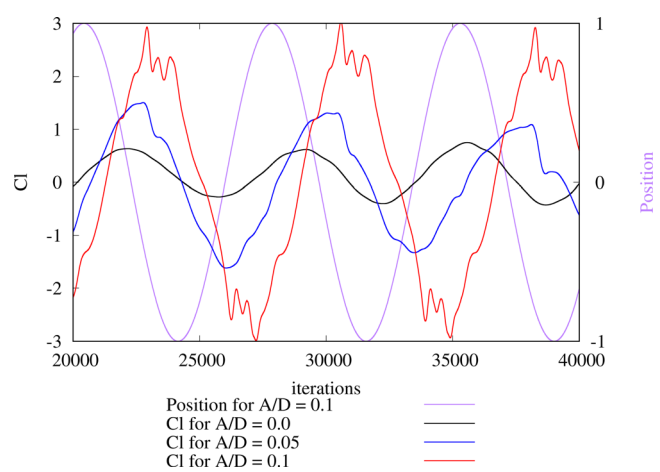

FIG. 11. Time history of the lift coefficient and position of the cylinder for the static and oscillating cases.

implement a solid wall boundary condition, even in the presence of geometrical singularities such as sharp corners. Turbulent test cases have demonstrated that the present method is robust and accurate, since it is able to capture fine details of the generation of vorticity at the wall, but also the interactions of the separated shear layer with the wall via viscous and pressure effects, in both steady and oscillating cylinder cases.

ACKNOWLEDGMENTS

This work was performed using the ProLB software. Centre de Calcul Intensif d'Aix-Marseille is acknowledged for granting access to its high performance computing resources. Part of this research was supported by ANR, Renault, Airbus and SafranTech by the Industrial Chair Program ALBUMS (ANR-CHIND-18-ALBUMS).

DATA AVAILABILITY

The data that support the findings of this study are available from the corresponding author upon reasonable request.

REFERENCES

[1]A. Sengissen *et al.*, "Simulations of LAGOON landing-gear noise using lattice Boltzmann solver," AIAA Paper No. 2015-2993, 2015.
[2]D. Armstrong *et al.*, "Numerical simulations of flow over a landing gear with noise reduction devices using the lattice-Boltzmann method," AIAA Paper No. 2013-2114, 2013.
[3]R. Bonnerot and P. Jamet, "Numerical computation of the free boundary for the two-dimensional Stefan problem by space-time finite elements," J. Comput. Phys. **25**(2), 163–181 (1977).
[4]H. M. Ettouney and R. A. Brown, "Finite-element methods for steady solidification problems," J. Comput. Phys. **49**(1), 118–150 (1983).
[5]M. Meldi, E. Vergnault, and P. Sagaut, "Lagrangian–Eulerian approach for the simulation of immersed moving solids with lattice Boltzmann method," J. Comput. Phys. **235**, 182–198 (2013).
[6]E. K. Fari, M. Geier, and M. Krafczyk, "Simulation of rotating objects in fluids with the cumulant lattice Boltzmann model on sliding meshes," Comput. Math. Appl. **79**, 3–16 (2020).
[7]P. Lallemand and L.-S. Luo, "Lattice Boltzmann equation with overset method for moving objects in two-dimensional flows," J. Comput. Phys. **407**, 109223 (2020).
[8]H. Yoo *et al.*, "A hybrid recursive regularized lattice Boltzmann model with overset grids for rotating geometries," Phys. Fluids **33**, 057113 (2021).
[9]C. S. Peskin, "Flow patterns around heart valves: A numerical method," J. Comput. Phys. **10**(2), 252–271 (1972).
[10]Z.-G. Feng and E. E. Michaelides, "The immersed boundary-lattice Boltzmann method for solving fluid-particles interaction problems," J. Comput. Phys. **195**(2), 602–628 (2004).
[11]L. Zhu *et al.*, "An immersed boundary method based on the lattice Boltzmann approach in three dimensions, with application," Comput. Math. Appl. **61**(12), 3506–3518 (2011).
[12]J. Favier, A. Revell, and A. Pinelli, "A lattice Boltzmann–immersed boundary method to simulate the fluid interaction with moving and slender flexible objects," J. Comput. Phys. **261**, 145–161 (2014).
[13]Z. Li *et al.*, "An immersed boundary-lattice Boltzmann method for single- and multi-component fluid flows," J. Comput. Phys. **304**, 424–440 (2016).
[14]M. Pepona and J. Favier, "A coupled immersed boundary–lattice Boltzmann method for incompressible flows through moving porous media," J. Comput. Phys. **321**, 1170–1184 (2016).
[15]S. Zhang, J. Zhou, and C. Shao, "Numerical investigation on yielding phenomena of magnetorheological fluid flowing through microchannel governed by transverse magnetic field," Phys. Fluids **31**(2), 022005 (2019).
[16]A. Coclite *et al.*, "A lattice Boltzmann dynamic-immersed boundary scheme for the transport of deformable inertial capsules in low-Re flows," Comput. Math. Appl. **80**(12), 2860–2876 (2020).
[17]X. Wu, Y. Li, and S. Zhou, "Flow-induced vibration on isolated and tandem elliptic cylinders with varying reduced velocities: A lattice Boltzmann flux solver study with immersed boundary method," Eur. J. Mech.-B/Fluids **89**, 45–63 (2021).
[18]E. Constant *et al.*, "An immersed boundary method in OpenFOAM: Verification and validation," Comput. Fluids **157**, 55–72 (2017).
[19]S. Wilhelm, J. Jacob, and P. Sagaut, "An explicit power-law-based wall model for lattice Boltzmann method-Reynolds-averaged numerical simulations of the flow around airfoils," Phys. Fluids **30**, 065111 (2018).
[20]B. Shi *et al.*, "Wall-modeling for large-eddy simulation of flows around an axisymmetric body using the diffuse-interface immersed boundary method," Appl. Math. Mech. **40**, 305–320 (2019).
[21]S. Kang, "An improved near-wall modeling for large-eddy simulation using immersed boundary methods," Int. J. Numer. Methods Fluids **78**, 76 (2015).
[22]S. Wang *et al.*, "A large eddy simulation of flows around an underwater vehicle model using an immersed boundary method," Theor. Appl. Mech. Lett. **6**, 302–305 (2016).
[23]F. Capizzano, "Coupling a wall diffusion model with an immersed boundary technique," AIAA J. **54**, 728–734 (2016).
[24]M. Ma, C. X. Huang, and W. X. Xu, "A dynamic wall model for large eddy simulation of turbulent flow over complex moving boundaries based on the immersed boundary method," Phys. Fluids **31**, 115101 (2019).
[25]F. Tessicini *et al.*, "Wall modeling for large-eddy simulation using immersed boundary method," Center for Turbulence Research-Annual Research Briefs (2002), pp. 181–187.
[26]C. Brehm, O. Browne, and N. Ashton, "Towards a viscous wall model for immersed boundary methods," AIAA Paper No. 2018–1560, 2018.
[27]M. Chavez-Modena *et al.*, "Simulations of aerodynamic separated flows using the lattice Boltzmann solver X flow," Energies **13**, 5146 (2020).
[28]J. Jacob, O. Malaspinas, and P. Sagaut, "A new hybrid recursive regularised Bhatnagar–Gross–Krook collision model for lattice Boltzmann method-based large eddy simulation," J. Turbul. **19**(11–12), 1051–1076 (2018).
[29]C. Coreixas *et al.*, "Recursive regularization step for high-order lattice Boltzmann methods," Phys. Rev. E **96**(3), 033306 (2017).
[30]J. Jacob and P. Sagaut, "Wind comfort assessment by means of large eddy simulation with lattice Boltzmann method in full scale city area," Build. Environ. **139**, 110–124 (2018).
[31]L. Merlier, J. Jacob, and P. Sagaut, "Lattice-Boltzmann large-eddy simulation of pollutant dispersion in complex urban environment with dens gas effects: Model evaluation and flow analysis," Build. Environ. **148**, 634–652 (2019).
[32]Y. Feng *et al.*, "Hybrid recursive regularized lattice Boltzmann simulation of humid air with application to meteorological flows," Phys. Rev. E **100**(2), 023304 (2019).
[33]Y. Feng *et al.*, "Hybrid recursive regularized thermal lattice Boltzmann model for high subsonic compressible flows," J. Comput. Phys. **394**, 82–99 (2019).
[34]S. Guo *et al.*, "An efficient lattice Boltzmann method for compressible aerodynamics on D3Q19 lattice," J. Comput. Phys. **418**, 109570 (2020).
[35]E. Leveque *et al.*, "Shear-improved Smagorinsky model for large-eddy simulation of wall-bounded turbulent flows," J. Fluid Mech. **570**, 491–502 (2007).
[36]S. Gsell, U. D'Ortona, and J. Favier, "Explicit and viscosity-independent immersed-boundary scheme for the lattice Boltzmann method," Phys. Rev. E **100**(3), 033306 (2019).
[37]W.-H. Hucho and G. Sovran, "Aerodynamics of road vehicles," Annu. Rev. Fluid Mech. **25**, 485–537 (1993).
[38]M. Roumeas, P. Gillieron, and A. Kourta, "Drag reduction by flow separation control on a car after body," Int. J. Numer. Methods Fluids **60**, 1222–1240 (2009).
[39]D. D. Chao and C. P. van Dam, "Airfoil drag prediction and decomposition," J. Aircr. **36**, 675–681 (1999).
[40]F. Noca, D. Shiels, and D. Jeon, "A comparison of methods for evaluating time-dependent fluid dynamic forces on bodies, using only velocity fields and their derivatives," J. Fluids Struct. **13**, 551–578 (1999).
[41]E. Guilmineau and P. Queutey, "A numerical simulation of vortex shedding from an oscillating cylinder," J. Fluids Struct. **16**(6), 773–794 (2002).

[42]A. Ongoren and D. Rockwell, "Flow structure from an oscillating cylinder Part 1. Mechanisms of phase shift and recovery in the near wake," J. Fluid Mech. **191**, 197–223 (1988).
[43]A.-H. Pham *et al.*, "Laminar flow past an oscillating circular cylinder in cross flow," J. Mar. Sci. Technol. **18**, 361–368 (2010).
[44]D. A. Lyn *et al.*, "A laser-Doppler velocimetry study of ensemble-averaged characteristics of the turbulent near wake of a square cylinder," J. Fluid Mech. **304**, 285–319 (1995).
[45]W. Rodi *et al.*, "Status of large eddy simulation: Results of a workshop," J. Fluids Eng. **119**, 248–262 (1997).
[46]E. Buffa, J. Jacob, and P. Sagaut, "Lattice-Boltzmann-based large-eddy simulation of high-rise building aerodynamics with inlet turbulence reconstruction," J. Wind Eng. Ind. Aerodyn. **212**, 104560 (2021).
[47]P. W. Bearman and E. D. Obasaju, "An experimental study of pressure fluctuations on fixed and oscillaing square-section cylinders," J. Fluid Mech. **119**, 297–321 (1982).
[48]P. W. Bearman and S. C. Luo, "Investigation of the aerodynamic instability of a square-section cylinder by forced oscillation," J. Fluids Struct. **2**, 161–176 (1988).
[49]Y. Z. Liu *et al.*, "A new modeling approach for transversely oscillating square-section cylinders," J. Fluids Struct. **81**, 492–513 (2018).
[50]M. H. Hirata *et al.*, "High Reynolds number oscillations of a circular cylinder," J. Braz. Soc. Mech. Sci. Eng. **30**, 304–312 (2008).
[51]E. D. Obasaju, "Forced-vibration study of the aeroelastic instability of a square-section cylinder near vortex resonance," J. Wind Eng. Ind. Aerodyn. **12**, 313–327 (1983).